Primary edge localized mode filament structure in the National Spherical Torus Experiment[a]

R. J. Maqueda,[1,b] R. Maingi,[2] and NSTX team

[1]*Nova Photonics, Inc., Princeton, New Jersey 08540, USA*
[2]*Oak Ridge National Laboratory, Oak Ridge, Tennessee 37830, USA*

Edge localized modes (ELMs) are routinely seen in the National Spherical Torus Experiment (NSTX) [M. Ono, Nucl. Fusion **40**, 557 (2000)]. These unstable modes give rise to plasma filaments that burst radially outward during the nonlinear phase of the instability, moving across flux surfaces into the scrape-off layer. Fast-frame visible imaging is used in NSTX to study the evolution and characteristics of the post-ELM filaments. These edge filaments, which are well aligned with the local magnetic field, are seen to evolve from a perturbation of the edge that within $40-50$ μs develops into the relatively high density/temperature primary filaments. The distribution of primary filaments in toroidal angle is seen to agree with a random model with moderate average toroidal mode numbers. At the same time, gas puff imaging shows that the perturbation of the edge leading to the burst of the ELM into the scrape-off layer is characterized by a broadband increase in fluctuations at much smaller poloidal wavelengths ($\lambda_{pol} \sim 2-12$ cm). These two measurements suggest that early development of turbulence may play a role in the development of primary ELM filamentation. © *2009 American Institute of Physics*. [DOI: 10.1063/1.3085798]

I. INTRODUCTION

Instabilities periodically develop near the edge of tokamak plasmas due to the large pressure gradients present during H-mode operation.[1] These instabilities, generally known as edge localized modes (ELMs),[2,3] result in submillisecond bursts of energy and particles that are lost from the closed field line region and, eventually, reach the plasma facing components (PFCs) where they may affect the lifetime of the material walls. Conversely, the technical limitations of the PFCs impose a limit on the power flux that can be tolerated in large devices like ITER. As an example, the current ITER design has adopted a 0.5 MJ/m^2 limit for the maximum allowed energy load over any 250 μs period to its PFCs in the divertor region.[4] The actual energy (or power) loads present during ELMs depend on the detailed distribution, both in time and space, of these losses. Although this energy load limit is a very stringent constraint on the size of the ELMs that can be allowed in ITER, the fine structure and dynamics of the energy (and particle) losses during ELMs in current experiments is not completely understood.

Experiments in a large number of tokamak devices have observed that the ELM evolves into filaments that are aligned with the local magnetic field, are radially and poloidally localized, and propagate radially and toroidally in the scrape-off layer (see Refs. 5–10, and references within). Furthermore, it has been shown that these filaments can be separated into two groups: high density and temperature primary filaments originating with the instability driving the ELM and lower density and temperature secondary filaments born from an increased level of turbulence present near the edge soon after the ELM onset.[11,12]

This paper describes the structure of the primary ELM filaments and their link to the instability driving the ELM. It is important then that the primary filaments be distinguished from the secondary filaments since the latter are not a consequence of the instability driving the ELM but a secondary effect of the ELM: an increased level of intermittent transport in the form of convective, filamentary cells.[13,14] Secondary filaments occur during an extended period of time, which depends on the ELM size, as compared to the primary filaments which are only present during the first ~ 40 μs of the ELM burst.[12] The primary filaments also propagate in the scrape-off layer with high radial velocities (up to 10 km/s) compared to the secondary filaments (1–2 km/s), and result in high localized power loads on PFCs of the main chamber,[15] away from the divertor region, as well as on those of the divertor target plates.[16,17]

Currently it is thought that a peeling-ballooning mode is responsible for the ELM onset,[18,19] at least for large size ELMs, with the models predicting that intermediate toroidal mode numbers ($n \sim 10-25$) will be unstable for large type I ELMs. Both smaller and larger mode numbers ($n \sim 3-5$, $n > 30$) could be present in smaller ELMs, provided that the smaller mode numbers (larger numbers) have a pure peeling (ballooning) drive.[19,20] If the growth rate of one particular mode number dominates over those of all other mode numbers the unstable peeling-ballooning mode nonlinearly evolves into a corresponding number of field-aligned primary filaments (cf. Fig. 5 of Ref. 18). A similar picture is presented in Fig. 1 of Ref. 3 for the case of a peeling instability driving a medium size type III ELM.

While some experimental data for large ELMs is consistent with the peeling-ballooning stability diagram,[16] the primary filaments originating in the nonlinear evolution of the ELM have also been used in the past to provide experimental

---

support for the models used to study the onset of the ELM phenomena. This experimental support can be best described as "counting" the number of filaments present within a given toroidal section of the device and, in this way, obtain the "toroidal quasimode number."[16] In some cases, this experimental mode number has been compared with the result (i.e., the most unstable toroidal mode number) yield by the model.[18]

If however, a broadband of toroidal mode numbers is unstable with similar growth rates, the nonlinear evolution is dominated by coupling between different modes, and beating between these modes results in a much smaller number of primary filaments (cf. Fig. 2 of Ref. [18]). If such is the case, "counting" of filaments is complicated by the constructive (and destructive) interference between modes.

In this paper we present imaging and analysis results during primary ELM filament formation in the National Spherical Torus Experiment[21] (NSTX) that support an additional alternative to the development of these primary filaments: the appearance of turbulence triggered by the unstable edge mode appears to play a dominant role in the formation of the primary filaments. The NSTX device and diagnostic setup is presented in Sec. II and the results and analysis are described in Sec. III. This paper concludes with a summary and discussion in Sec. IV.

II. EXPERIMENTAL SETUP

Type III ELMs present in the NSTX (Ref. [21]) were used for the work presented here. This experiment is a low aspect ratio tokamak with a major radius $R = 0.86$ m and a minor radius $a = 0.67$ m. A plasma current of $I_p = 800$ kA, a toroidal field on axis of $B_t = 0.45$ T and an elongation of $\kappa \sim 1.9$ were used in a magnetic topology close to double null, although slightly biased toward the lower divertor. A regime with periodic type III ELMs (frequency of ~ 460 Hz) was achieved by adjusting the auxiliary heating power by means of neutral beam injection to ~ 2 MW, just above the *L-H* transition power threshold for these plasmas. The resulting energy loss per ELM was $\Delta W_{ELM}/W_{ped} \sim 5\%$, the normalized electron collisionality at the pedestal $\nu_e^* \sim 1.3$ and the Greenwald density fraction $n_e/n_G \sim 0.5$. The classification of these ELMs in the type III category is based on their size and frequency scaling with the auxiliary heating power and line averaged density.[22]

The main diagnostic used in the work presented in this paper was high frame rate imaging in the visible range of wavelengths. Two fast-framing digital cameras were employed, each capturing 121 212 frames/s yielding an interframe time of 8.25 μs. The frame exposures used were 5–6 μs.[23] One of the cameras, a Phantom 7.3 from Vision Research, was used in a wide angle, fish-eye elevation view of the plasma which covered about 90% of the plasma cross section, centered up and down respect to the device midplane. Although no interference filter was used in the optical path of this camera, other experience shows that most of the emission recorded corresponds to deuterium line emission from the edge and scrape-off layer.

The other camera (a Phantom 7.1) viewed a tangential, small-field view of a ~ 25 cm poloidal section of the edge just above the outer midplane of the plasma. The pitch angle of the magnetic field in the viewing region of this tangential edge camera was selected so that the visible light emission was viewed along the direction of the local magnetic field line. In this way, "end-on" images of the field-aligned edge structure and filaments were obtained. In addition, a nonperturbing deuterium gas puff (~ 10 Torr l/s) was added in the field of view of the small-field camera to further localize the emitting region to an ~ 20 cm length along the line of sight and also increase the contrast and brightness of the D_α line emission which was selected with a narrowband interference filter. Degas 2 simulation of the D_α emission in this diagnostic setup indicates that the spatial structure of the emitting neutral cloud captured in the camera images reflects the structure of the plasma, despite a nonlinear dependence of the emission on the electron density and temperature of this plasma.[24] Further details of this gas puff imaging (GPI) diagnostic, as well as of the nonperturbing condition of the gas puff itself, can be seen in Refs. [25] and [26].

The D_α emission seen by the small-field camera, integrated over the whole image, was used to define the ELM burst time (t_{ELM}) as the time when this time series crosses a predetermined threshold level. This signal (with ~ 120 kHz sampling rate) has a faster response time to the ELM onset than the traditional lower divertor D_α emission generally used in literature. Finally, even though the cameras were run independently with no frame synchronization, the overlapping fields of view were employed to maintain a cross-reference between the two independent time bases and correct for any slow time drifts between them.

III. PRIMARY FILAMENT STRUCTURE

The development of a primary ELM filament in the edge of NSTX is shown in Fig. 1. This sequence of images was obtained using the tangential, small-field-of-view camera and each frame displays an approximately 25×25 cm^2 portion of the poloidal plane (radial versus poloidal), just above the outer midplane. A deuterium gas puff is being injected from the right in these images. Given the high pitch angle of the magnetic field in low field side of NSTX, this 25 cm poloidal length maps into ~ 45 cm of toroidal extent (or $\sim 17°$ in toroidal angle). The solid line in these frames indicates the approximate position of the separatrix and the dotted line represents the shadow of the limiter.

A perturbation is seen in Fig. 1 growing from the unperturbed *H*-mode edge,[25] present 50 μs before the ELM burst time (t_{ELM}), until a filament has formed in the scrape-off layer (SOL) 8 μs after this ELM time. Given the observation angle, which is approximately aligned with the local magnetic field at the gas puff, together with the localization along the line of sight provided by this puff, this filament is seen as a plasma "blob" instead of a helical structure. Once in the SOL the primary ELM filaments either break up into a finer, smaller scale-size blobs before dissipating within the SOL or propagate radially (and toroidally), reaching in many occasions beyond the shadow of the limiter.[12]
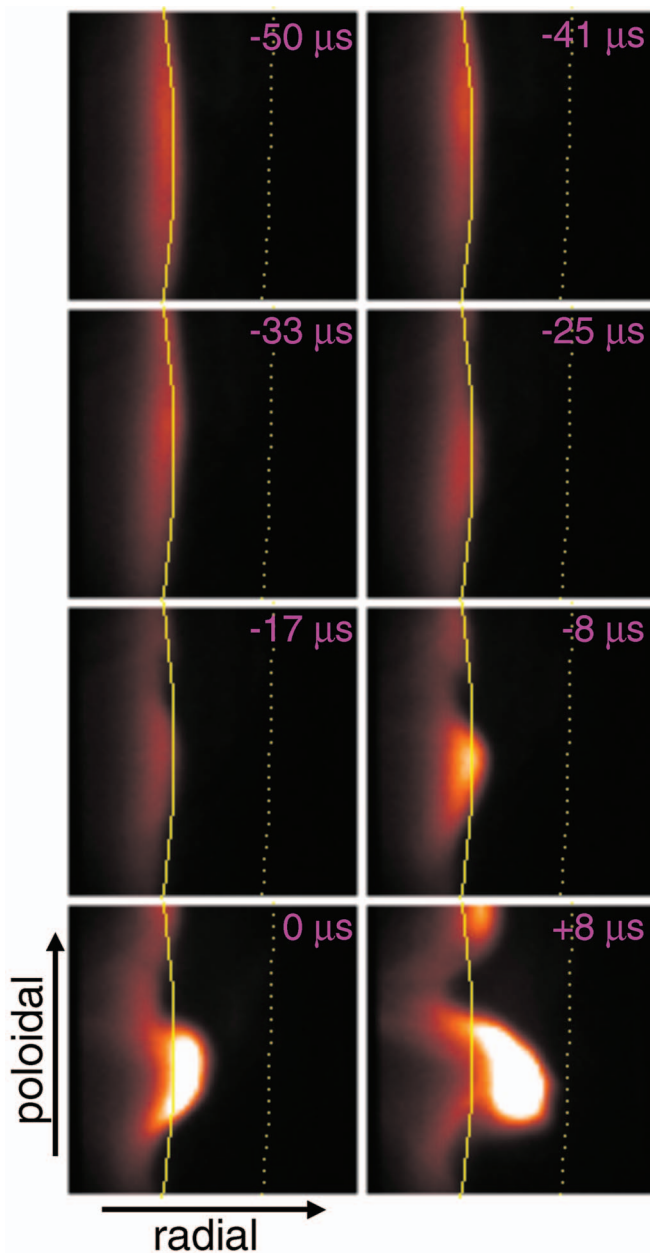
FIG. 1. (Color) Sequence of gas puff imaging frames showing the development of a primary filament during a type III ELM. False color images of D_α emission from a 25 cm (radial) $\times$ 25 cm (poloidal) portion of the low field side edge. The separatrix is indicated with a solid line and the limiter shadow is shown by the dotted line. The times indicated are relative to the ELM time t_{ELM} (shot 124667, $t_{ELM} = 267.32$ ms).
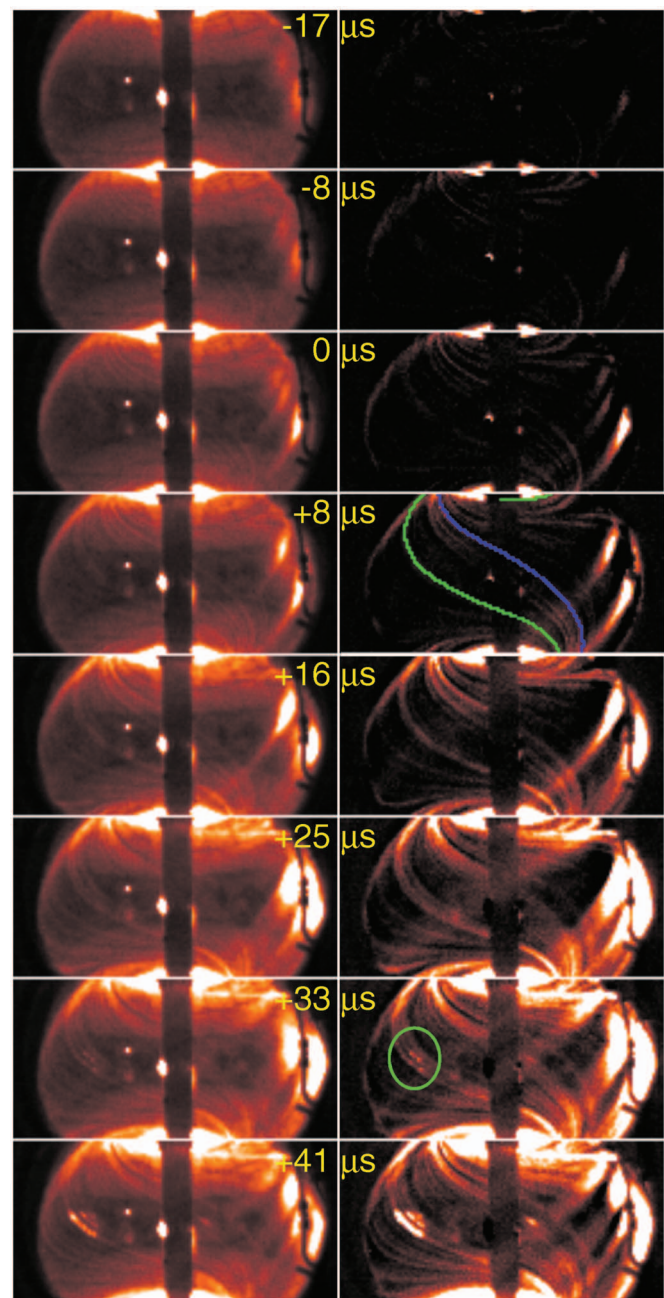

FIG. 2. (Color) Sequence of wide-angle-view images showing an increasing number of primary filaments during the same type III ELM as in Fig. 1. These false color images were obtained without interference filter and display raw frames on the left column and contrast enhanced images (average inter-ELM image subtracted) on the right column. The times indicated are relative to the ELM time.

The global structure and distribution of the primary filaments can be observed with the wide angle imaging camera. A sequence of images corresponding to the same ELM as that shown in Fig. 1 can be seen in Fig. 2. In this figure raw images are shown on the left column and contrast enhanced images, by subtracting an average inter-ELM image, are displayed in the right column. The overall spherical shape of the NSTX's plasmas can be seen in these images together with the 37 cm diameter center column. The high field side fuelling puff located at the midplane of the device can be seen on the left side of the center column.

Together with the start of the ELM an increasing number of filaments can be seen in Fig. 2, including some in the near field of the imaging system. In particular, the frames at 0 and 8 μs show toward the right edge of the images the same filaments as those displayed in Fig. 2 at these same times relative to the ELM time. These filaments, with their D_α emission enhanced by the GPI deuterium puff, are imaged "end-on" in Fig. 1.

The contrast enhanced frame in Fig. 2 at +8 μs shows the overlay of two magnetic field lines. As can be seen here, and widely published in the literature,[5,8] these filaments are aligned with the local magnetic field. They are located in the

SOL, open field line region and extend beyond the high shear region near the *X*-point, reaching the divertor target plates.[16] Although the radial and toroidal position of the primary filaments can be tracked from frame to frame by matching their images with particular magnetic field line overlays (as shown in Fig. 2), the close fitting stabilizing plates in NSTX (outer gaps of <10 cm) prevent such tracking to be done for more than a few frames before the filaments make contact with the material wall. Using the GPI setup the radial velocity of these filaments was reported in Ref. 12 to be up to 8 km/s. At the same time, the toroidal velocities were measured to be as high as 20 km/s, equivalent to poloidal velocities of <11 km/s. This toroidal rotation is in the same direction as the rotation of the core plasma in NSTX.

While the number of filaments seen in the wide angle, global view of NSTX increases with time during the early stages on the ELM evolution (Fig. 2), several different phenomena affect the number of filaments being observed. In first place, due to breakup and dispersal of the filament and/or recycling of loosely bound particles at the plasma facing components as the filaments interact with them, individual nearby filaments can coalesce into a larger size filament. Such is the case of the group of three filaments observed in Fig. 2, frame at +8 μs (the right most of this group being the one overlaid with the blue field line). In the frame at 33 μs, this group appears as a single, wider filament.

Conversely, as a filament propagates in the SOL it can break or generate separate substructures. An example of this is seen in the evolution of the filament indicated with the green field line in Fig. 2. This filament, while propagating toroidally and finally interacting with the PFC in the frame at 41 μs, gives rise to a few additional filaments as seen, for instance, in the frame at 33 μs (portion of image highlighted with a circle). A similar phenomenon, i.e., the increase in the effective toroidal mode number, was observed by Neuhauser *et al.* in ASDEX Upgrade and reported in Ref. 9. Finally, it should be pointed out, the presence of secondary ELM filaments originating in the confinement degradation due to the ELM, as presented in Ref. 12, can be misinterpreted as an increase in the number of primary filaments and an additional increase in the toroidal quasimode number.

The toroidal angle distribution of the primary filaments observed during type III ELMs can be measured by selecting, from each ELM, an appropriate wide angle camera image. Such image has to be close to the ELM time allowing time for the primary filaments to develop but before these filaments coalesce as described above, and before secondary filaments start developing in the SOL (see Fig. 4 of Ref. 12). This frame is generally within 16 μs of the ELM time (for example, frame at 0 μs for the ELM shown in Figs. 1 and 2). The toroidal angle of these filaments is then identified by overlaying a magnetic field line and the distances between consecutive filaments can then be measured. The probability density function for these toroidal angular distances obtained from a large number of filaments is shown by a solid line in Fig. 3.

A few observations can be made regarding the experimental probability density function shown in Fig. 3 (solid line). First, there is no distinct periodic mode structure but a
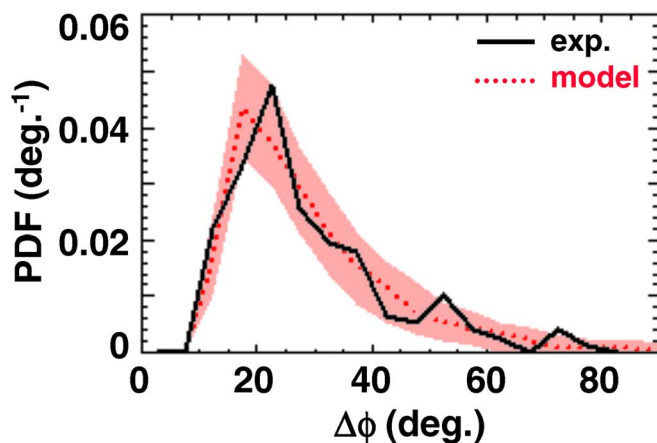

FIG. 3. (Color online) Probability density function of toroidal angle separations between primary filaments during type III ELMs. The solid line shows experimental data and the dotted line (and shaded region) indicates results from model described in text. A total of 179 filaments were extracted from a sequence of 24 similar type III ELMs.

wide peak centered at about 20° of toroidal separation. The width of this peak is, on the other hand, substantially larger than the experimental resolution of the imaging (~2° in toroidal angle). Second, there is a minimum toroidal separation between filaments of ~12°. This minimum is not due to diagnostic limitations but an intrinsic characteristic of the primary filaments. Not only is the resolution of the wide imaging smaller than this minimum but also the GPI setup has an even smaller angular resolution, and as described below, does not see the formation of primary filaments with small toroidal separations.

The experimental probability density function (PDF) is compared in Fig. 3 with the results of a simple model in which a number of filaments are distributed randomly in toroidal angles. The only departure from this uniform random distribution is an imposed lower limit in the possible separations between filaments. In this model, filaments that are randomly placed within this lower separation limit are "coalesced" into a single filament located at their average toroidal angle. In the particular realization of the model shown with a dotted line in Fig. 3 the PDF was been obtained from 416 "ELMs," each of them having 24 filaments (randomly distributed within the 360° toroidally). The minimum angular separation allowed in the model results shown was 13°. Filament coalescence results in the average number of filaments per ELM to be reduced from the $n=24$ specified to $n \sim 12.2(\sim 51\%)$.

Since the number of filaments available from the experimental measurements is limited, the model was also used to analyze the magnitude of the sampling error. For this purpose, 1000 model realizations with a similar number of filaments as those measured were run and the histograms of their angular separations were analyzed statistically. For each angular separation the shaded region in Fig. 3 indicates the 5–95 percentile range for this collection of 1000 histograms. As it can be seen in this figure, there is a good confidence that the experimental PDF matches that of the model and not just a chance coincidence.
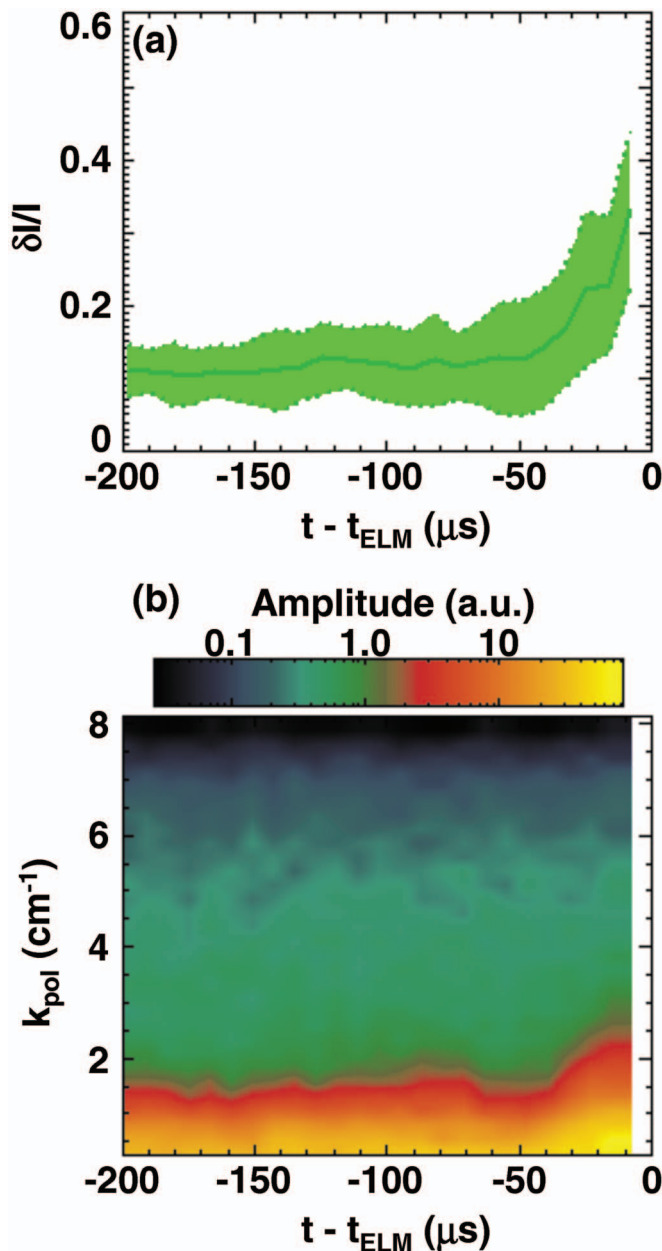
FIG. 4. (Color) Characteristics of the time evolution of the edge leading to type III ELMs: (a) relative fluctuation level (rms) and (b) poloidal amplitude spectrum. The ELM perturbation is seen to locally start 40–50 μs before the ELM crash occurring at t_{ELM}. The edge structure (2–3 cm inside the separatrix) is measured with the GPI diagnostic and is averaged over 19 similar type III ELMs.

The structure of the edge plasma leading to the burst of type III ELMs into the scrape-off layer, as measured with the gas puff imaging diagnostic, is shown in Fig. 4. The analysis shown in this figure corresponds to poloidal line outs in the images at the peak in the D_α emission region which is located $\sim$3 cm inside the separatrix (see Fig. 1, for example), typically at the foot of the pedestal. Although the mode driving the ELM may be, according to models, initially located further up in the pedestal, the mode grows affecting the foot of this pedestal in a short period of time as can be seen in Figs. 2 and 5 of Ref. 18 (peeling-ballooning model) or Fig. 1 of Ref. 3 (peeling model). Consequently, the measurement

with the GPI setup at the foot of the pedestal should reflect the growth of the driving mode even if it initially located at a smaller radius.

Before the ELM the edge emission is characterized by a 10% root-mean-square (rms) fluctuation level [Fig. 4(a)] and a broadband poloidal wave-number spectrum [Fig. 4(b)], peaking toward low k_{pol} (i.e., long wavelengths). These are typical characteristics for an H-mode edge obtained with a moderate amount auxiliary heating power (2 MW).[26] Approximately 40–50 μs before the ELM burst at $t=t_{ELM}$, the edge of the plasma, where the D_α emission originates, shows an increase in fluctuation levels and increase in the spectrum amplitudes localized to low poloidal wave numbers (k_{pol} <3 cm^{-1}).

The data in Fig. 4 are obtained from an average over 19 similar type III ELMs, including the one shown in Figs. 1 and 2. In general, in a similar way as Fig. 1, only one primary filament develops within the 25 cm of poloidal coverage of the GPI diagnostic. Since this poloidal distance corresponds to 17° of toroidal angle, this observation is then consistent with the minimum separation distance discussed in connection to Fig. 3. It should be pointed out, that the D_α emission in the scrape-off layer quickly evolves (within a few camera frames, <20 μs) into a set of substructures resulting from the breakup of primary filaments. For example, the primary filament seen in Fig. 1 breaks up in this way as soon as it completes it separation from the edge (t-t_{ELM} =16 μs). Another primary filament enters the field of view of the camera from the top and propagates radially and poloidally beyond the shadow of the limiter before breaking up.

Finally, and most importantly, the increase in spectral amplitudes at long wavelengths as the ELM develops within the separatrix shows no particular mode structure. Nevertheless this increase, as indicated earlier, affects low poloidal wave numbers only and does not extend to higher k_{pol} values. This observation is consistent with the broad probability density function shown in Fig. 3. It should be pointed out, though, that the limited spatial coverage of the GPI diagnostic imposes an upper bound on the wavelengths accessible to $\lambda_{pol}\sim$ 12 cm, corresponding to $\sim$9° of toroidal angle.

IV. SUMMARY AND DISCUSSION

Primary ELM filaments are seen developing in the scrape-off layer of NSTX. The original goal of the measurements presented here was to measure the development and characteristics of the mode driving the ELM and the subsequent formation of these primary filaments. Even though in some occasions the gas puff imaging results showed the formation of a filament following the development of what can be interpreted as a "ballooning" structure (and example shown in Fig. 1), the general, most common result was an unstructured evolution into primary filamentation. Even in the case when a ballooning filament was formed, the corresponding wide angle view showed a nonperiodic filament structure, i.e., nonuniform toroidal angle separation between filaments (Fig. 2).

As a general result it can be said that the primary filaments, aligned with the local magnetic field, are distributed

in a nonperiodic structure within the toroidal circumference of NSTX. Similar to other experiments, one possible interpretation is that a mixture of toroidal mode numbers (Fig. 2 of Ref. 18) and not a single, dominating toroidal mode number (Fig. 5 of Ref. 18) is responsible, through their nonlinear phase, for the primary filaments observed in the scrape-off layer. It is this combination of modes what may lead to the broad distribution of toroidal separation between filaments. The distribution of angular distances between filaments, as shown in Fig. 3, is equivalent to that shown in Fig. 1(c) of Ref. 27 and the broadband distribution of filaments is also apparent in the images of Fig. 7 of Ref. 16. The large scatter in the measurements of the mode number has also been reported in Refs. 27 and 28. The experimental characterization of these earlier measurements has resulted, in turn, in the introduction in literature of the toroidal "quasimode" number.[9,16]

Nevertheless, it is shown in Sec. III that the probability density function obtained from the experiment matches well that obtained by the "random" model described. This introduces the alternative explanation that the formation of filaments does not have a direct relation to a single or a combination of periodic modes developing near the edge but to a broadband turbulent process that covers both long toroidal wavelengths (as seen in the wide angle view images and Fig. 3) and shorter wavelengths (GPI data, Fig. 4). The instability itself, for instance, the peeling-ballooning mode, is just the trigger mechanism for this turbulent process.

In the example shown in Fig. 1, a clear, well defined harmonic mode can be seen growing on the edge which then results in the formation of a primary filament. This sequence of images is, in itself, quite similar to the multimode case presented by Snyder et al. in Ref. 18. Nevertheless, this edge evolution is as pointed out above not the most common result. This can be seen by the broadband increase in the poloidal wave-number spectra shown in Fig. 4(b), and not just an increase at some characteristic k_{pol}. As discussed above, the nonlinear evolution appears to be more complicated than that resulting from the BOUT simulations presented in Ref. 18. The appearance of ELM filaments with a random angular distribution has yet to be simulated by models.

The presence of a lower angular separation limit, below which filaments either coalesce or simply form as a single filament, may be related to characteristic size of these structures and the formation process. It should be noted that this minimum is similar to the toroidal angle covered by the growing ballooning mode structure in Fig. 1. Then, if this formation process is governed by the profiles (like the pressure profile) at the edge regardless of the trigger mechanism, it dominates over a given toroidal length within which only one filament could result. The trigger could either be the periodic ballooning (or peeling) mode itself or a short-wavelength turbulent perturbation which then results in a broad distribution in the toroidal separation between primary filaments or, equivalently, a poorly defined experimental toroidal mode number. The later appears to be the case present in NSTX.

One of the characteristics of the primary ELM filaments, in comparison with the secondary filaments born from changes in confinement as a consequence of the ELM,[12] is that they are composed by plasma of higher density and/or temperature. This results then in a brighter D_α emission as seen in the GPI images.[24] The fact that primary filaments are only seen during early times during the ELM burst indicates that the top section of the pedestal with higher densities/temperatures is perturbed first by either the driving mode or the short-wavelength turbulence. This is then followed by the triggering of turbulence throughout the edge profile, including the bottom part of the pedestal where blobs (i.e., secondary ELM filaments) are formed.[29]

Finally, it should be pointed out that in some occasions a precursor filamentary structure (like that in Fig. 1 of Ref. 12) is seen during type III ELMs in NSTX. This filamentary structure has generally a low toroidal mode number ($n \sim 2-4$). A similar low mode number precursor has been seen in the magnetic signatures of long-lived precursors for type III ELMs in NSTX during other experiments.[22] Nevertheless, other primary filaments develop during the initial stages of the ELM burst. This mismatch between the mode number of the precursor and the quasimode number of the filaments has also been observed by Neuhauser et al.[9] The results and analysis shown in this paper suggest that although the driver for the ELM could be a low mode number instability, the subsequent primary filaments are consequence of induced turbulent processes which typically has a larger toroidal quasimode number.

ACKNOWLEDGMENTS

[1] ASDEX Team, Nucl. Fusion **29**, 1959 (1989).
[2] H. Zohm, Plasma Phys. Controlled Fusion **38**, 105 (1996).
[3] J. W. Connor, Plasma Phys. Controlled Fusion **40**, 191 (1998).
[4] W. Fundamenski, J. Nucl. Mater. **390–391**, 10 (2009).
[5] A. Kirk, N. Ben Ayed, G. Counsell, B. Dudson, T. Eich, A. Herrmann, B. Koch, R. Martin, A. Meakins, S. Saarelma, R. Scannell, S. Tallents, M. Walsh, H. R. Wilson, and the MAST team, Plasma Phys. Controlled Fusion **48**, B433 (2006).
[6] A. Herrmann, A. Kirk, A. Schmid, B. Koch, M. Laux, M. Maraschek, H. W. Mueller, J. Neuhauser, V. Rohde, M. Tsalas, E. Wolfrum, and ASDEX Upgrade Team, J. Nucl. Mater. **363–365**, 528 (2007).
[7] B. Kurzan, L. D. Horton, H. Murmann, J. Neuhauser, W. Suttrop, and the ASDEX Upgrade Team, Plasma Phys. Controlled Fusion **49**, 825 (2007).
[8] R. Scannell, A. Kirk, N. Ben Ayed, P. G. Carolan, G. Cunningham, J. McCone, S. L. Prunty, and M. J. Walsh, Plasma Phys. Controlled Fusion **49**, 1431 (2007).
[9] J. Neuhauser, V. Bobkov, G. D. Conway, R. Dux, T. Eich, M. Garcia-Munoz, A. Herrmann, L. D. Horton, A. Kallenbach, S. Kalvin, G. Kocsis, B. Kurzan, P. T. Lang, M. Marascheck, H. W. Mueller, H. D. Murmann, R. Neu, A. B. Peeters, M. Reich, V. Rohde, A. Schmid, W. Suttrop, M. Tsalas, W. Wolfrum, and the ASDEX Upgrade Team, Nucl. Fusion **48**, 045005 (2008).
[10] A. Schmid, A. Herrmann, H. W. Müller, and the ASDEX Upgrade Team, Plasma Phys. Controlled Fusion **50**, 045007 (2008).
[11] J. L. Terry, I. Cziegler, A. E. Hubbard, J. A. Snipes, J. W. Hughes, M. J.

Greenwald, B. LaBombard, Y. Lin, P. Phillips, and S. Wukitch, J. Nucl. Mater. **363–365**, 994 (2007).

[12] R. J. Maqueda, R. Maingi, and J.-W. Ahn, J. Nucl. Mater. **390–391**, 843 (2009).

[13] J. A. Boedo, D. L. Rudakov, E. Hollmann, D. S. Gray, K. H. Burrell, R. A. Moyer, G. R. McKee, R. Fonck, P. C. Stangeby, T. E. Evans, P. B. Snyder, A. W. Leonard, M. A. Mahdavi, M. J. Schaffer, W. P. West, M. E. Fenstermacher, M. Groth, S. L. Allen, C. Lasnier, G. D. Porter, N. S. Wolf, R. J. Colchin, L. Zeng, G. Wang, J. G. Watkins, T. Takahashi, and DIII-D Team, Phys. Plasmas **12**, 072516 (2005).

[14] R. A. Pitts, P. Andrew, G. Arnoux, T. Eich, W. Fundamenski, A. Huber, C. Silva, D. Tskhakaya, and JET EFDA Contributors, Nucl. Fusion **47**, 1437 (2007).

[15] E. Gauthier, P. Andrew, G. Arnoux, Y. Corre, and H. Roche, J. Nucl. Mater. **363–365**, 1026 (2007).

[16] T. Eich, A. Herrmann, J. Neuhauser, R. Dux, J. C. Fuchs, S. Günter, L. D. Horton, A. Kallenbach, P. T. Lang, C. F. Maggi, M. Marascheck, V. Rohde, W. Schneider, and the ASDEX Upgrade Team, Plasma Phys. Controlled Fusion **47**, 815 (2005).

[17] A. Kirk, G. F. Counsell, G. Cunningham, J. Dowling, M. Dunstan, H. Meyer, M. Price, S. Saarelma, R. Scannell, M. Walsh, H. R. Wilson, and the MAST team, Plasma Phys. Controlled Fusion **49**, 1259 (2007).

[18] P. B. Snyder, H. R. Wilson, and X. Q. Xu, Phys. Plasmas **12**, 056115 (2005).

[19] H. R. Wilson, S. C. Cowley, A. Kirk, and P. B. Snyder, Plasma Phys. Controlled Fusion **48**, A71 (2006).

[20] S. Saarelma, T. C. Hender, A. Kirk, H. Meyer, H. R. Wilson, and MAST Team, Plasma Phys. Controlled Fusion **49**, 31 (2007).

[21] M. Ono, S. M. Kaye, Y.-K. M. Peng, G. Barnes, W. Blanchard, M. D. Carter, J. Chrzanowski, L. Dudek, R. Ewig, D. Gates, R. E. Hatcher, T. Jarboe, S. C. Jardin, D. Johnson, R. Kaita, M. Kalish, C. E. Kessel, H. W. Kugel, R. Maingi, R. Majeski, J. Manickam, B. McCormack, J. Menard, D. Mueller, B. A. Nelson, B. E. Nelson, C. Neumeyer, B. Oliaro, F. Paoletti, R. Parsells, E. Perry, N. Pomphrey, S. Ramakrishnan, R. Raman, G. Rewoldt, J. Robinson, A. L. Roquemore, P. Ryan, S. Sabbagh, D. Swain, E. J. Synakowski, M. Viola, M. Williams, J. R. Wilson, and NSTX Team, Nucl. Fusion **40**, 557 (2000).

[22] R. Maingi, C. E. Bush, E. D. Fredrickson, D. A. Gates, S. M. Kaye, B. P. LeBlanc, J. E. Menard, H. Meyer, D. Mueller, N. Nishino, A. L. Roquemore, S. A. Sabbagh, K. Tritz, S. J. Zweben, M. G. Bell, R. E. Bell, T. Biewer, J. A. Boedo, D. W. Johnson, R. Kaita, H. W. Kugel, R. J. Maqueda, T. Munsat, R. Raman, V. A. Soukhanovskii, T. Stevenson, and D. Stutman, Nucl. Fusion **45**, 1066 (2005).

[23] R. J. Maqueda, R. Maingi, K. Tritz, K. C. Lee, C. E. Bush, E. D. Fredrickson, J. E. Menard, A. L. Roquemore, S. A. Sabbagh, and S. J. Zweben, J. Nucl. Mater. **363–365**, 1000 (2007).

[24] D. P. Stotler, B. LaBombard, J. L. Terry, and S. J. Zweben, J. Nucl. Mater. **313–316**, 1066 (2003).

[25] R. J. Maqueda, G. A. Wurden, D. P. Stotler, S. J. Zweben, B. LaBombard, J. L. Terry, J. L. Lowrance, V. J. Mastrocola, G. F. Renda, D. A. D'Ippolito, J. R. Myra, and N. Nishino, Rev. Sci. Instrum. **74**, 2020 (2003).

[26] S. J. Zweben, R. J. Maqueda, D. P. Stotler, A. Keesee, J. Boedo, C. E. Bush, S. M. Kaye, B. LeBlanc, J. L. Lowrance, V. J. Mastrocola, R. Maingi, N. Nishino, G. Renda, D. W. Swain, and J. B. Wilgen, Nucl. Fusion **44**, 134 (2004).

[27] A. Kirk, H. R. Wilson, G. F. Counsell, R. Akers, E. Arends, S. C. Cowley, J. Dowling, B. Lloyd, M. Price, M. Walsh, and MAST Team, Phys. Rev. Lett. **92**, 245002 (2004).

[28] J. H. Yu, J. A. Boedo, E. M. Hollmann, R. A. Moyer, D. L. Rudakov, and P. B. Snyder, Phys. Plasmas **15**, 032504 (2008).

[29] J. R. Myra, D. A. D'Ippolito, D. P. Stotler, S. J. Zweben, B. P. LeBlanc, J. E. Menard, R. J. Maqueda, and J. Boedo, Phys. Plasmas **13**, 092509 (2006).